Chinese Chemical Letters 35 (2024) 109106

Contents lists available at ScienceDirect

Chinese Chemical Letters

journal homepage: www.elsevier.com/locate/cclet

Modulating the p-band center of carbon nanofibers derived from Co spin state as anode for high-power sodium storage

Zhijia Zhang[a,e,*], Yuwen Zhao[a], Yanhao Wei[a], Mengmeng Zhang[a,*], Chunsheng Li[b,c,*], Yan Sun[b,c], Jianmin Ma[d], Yong Jiang[a,e]

[a] School of Materials Science and Engineering, State Key Laboratory of Separation Membrane and Membrane Processes, Tiangong University, Tianjin 300387, China
[b] School of Chemistry and Life Sciences, Suzhou University of Science and Technology, Suzhou 215009, China
[c] Key Laboratory of Advanced Electrode Materials for Novel Solar Cells for Petroleum and Chemical Industry of China, Suzhou University of Science and Technology, Suzhou 215009, China
[d] School of Chemistry, Tiangong University, Tianjin 300387, China
[e] School of Electronic and Information Engineering, Institute of Quantum Materials and Devices, Tiangong University, Tianjin 300387, China

ARTICLE INFO

Article history:
Received 13 July 2023
Revised 31 August 2023
Accepted 14 September 2023
Available online 16 September 2023

Keywords:
Carbon nanofibers
Chemical vapor deposition
Spin state
p-band center
Sodium-ion battery

ABSTRACT

Carbon nanofibers (CNFs) have received extensive and in-depth studied as anodes for sodium-ion batteries (SIBs), and yet their initial Coulombic efficiency and rate capability remain enormous challenge at practical level. Herein, CNFs anchored with cobalt nanocluster (CNFs-Co) were prepared using chemical vapor deposition and thermal reduction methods. The as-prepared CNFs-Co shows a high initial Coulombic efficiency of 91% and a high specific discharge capacity of 246 mAh/g at 0.1 A/g after 200 cycles as anode for SIBs. Meanwhile, the CNFs-Co anode still delivers a high cycling stability with 108 mAh/g after 1000 cycles at 10 A/g. These excellent electrochemical properties could be attributed to the involved spin state Co, which endows CNFs with large interplanar spacing (0.39 nm) and abundant vacancy defects. Importantly, the spin state Co downshifts the p-band center of carbon and strengthens the Na^+ adsorption energy from −2.33 eV to −2.64 eV based on density functional theory calculation. This novel strategy of modulating the carbon electronic structure by the spin state of magnetic metals provides a reference for the development of high-performance carbon-based anode materials.

Currently, lithium-ion batteries (LIBs) have developed rapidly, expanding from portable electronic devices to emerging electric vehicles and smart grids [1,2]. Considering the scarcity of lithium resources, the rational development and utilization of the earth's abundant elements are urgent and of great significance [3,4]. Among the abundant elements in the earth's crust (O, Si, Al, Fe, Ca, Na, K, Mg, Ti, P, and Mn), the physical-chemical properties of sodium are closer to lithium than that of other elements. Therefore, rechargeable sodium-ion batteries (SIBs) might be a potential alternative to LIBs, which have received increasing research attention in recent years. Compared to LIBs, SIBs have lower capacity density and power density due to the large Na^+ size [4,5]. Meanwhile, Sodium ions are more difficult to participate in the charging and discharging processes due to their large size, which leads to poor electrochemical performance [6,7]. From the perspective of the LIBs history, the research on anode materials is of great significance for promoting their practical applications. Amorphous carbon-based anode materials feature large disorders which makes it possess high specific sodium storage capacity, low sodium storage potential, and excellent cycling stability, becoming as anode materials for SIBs. However, the low initial Coulombic efficiency and poor cycle performance cause difficulty in their practice applications [8,9].

Carbon nanofibers (CNFs) exhibit large specific surface area and porosity, thus exhibiting good sodium storage properties in carbonaceous materials [10–13]. For example, the fabricated CNFs *via* an electrospinning technique exhibit excellent cycle stability of 97.7% capacity retention rate after 200 cycles [14]. Furthermore, our previous work prepared braided porous carbon fibers by chemical vapor deposition (CVD), which exhibit an outstanding discharge capacity of 400 mAh/g at 0.1 A/g after 500 cycles [15]. These recently reported carbon anode materials have received substantial achievements. However, further improvements for CNFs are urgent and challenging, such as specific capacity, first cycle

* Corresponding authors.
E-mail addresses: zhangzhijia@tiangong.edu.cn (Z. Zhang), zhangmm912@tiangong.edu.cn (M. Zhang), lichsheng@163.com (C. Li).

https://doi.org/10.1016/j.cclet.2023.109106
1001-8417/

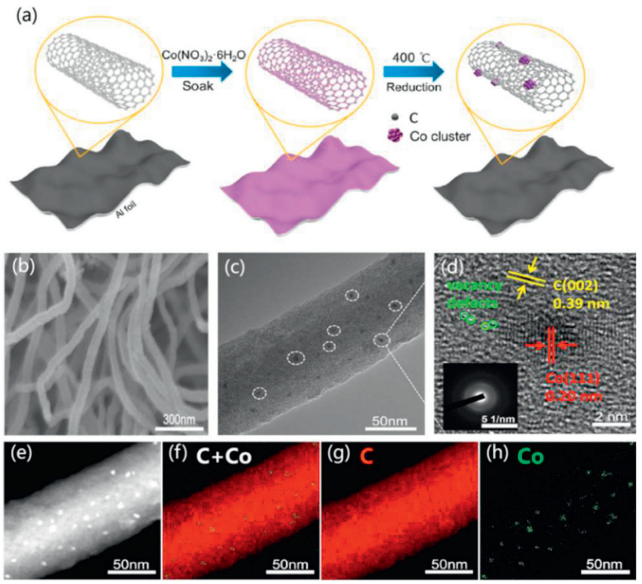

Fig. 1. Microstructure characterizations of CNFs-Co. (a) Synthetic process, (b) FE-SEM image, (c) TEM image, (d) HRTEM image (the inset is SAED pattern), and (e-h) element mapping.

Coulombic efficiency [16], and commercialization cost [17]. Thus, Ren *et al.* designed the channel structure to tune the microstructure of CNFs, which shows excellent cycle stability with a capacity retention rate of 90% after 300 cycles at 0.4 C [18]. Moreover, heteroatom doping can change the structural properties of hard carbon. For example, the doped P/S expanded its interplanar spacing and extended the capacity of the low-voltage platform, while the doped P/B increased the defect concentration leading to the higher inclined sloping sodiation capacity [19]. As an important strategy to improve the sodium storage performance of CNFs, heteroatom doping could change their microstructure and electronic state. And then, affecting their conductivity and defect content ultimately improved the sodium storage performance of CNFs [20].

In this study, CNFs with dense vacancies and uniform morphology were successfully synthesized by roll-to-roll plasma-enhanced CVD (RTR-PECVD) strategy, which are grown *in situ* on Al foil. CNFs anchored with Co nanocluster (CNFs-Co) were prepared through a simple thermal reduction method that reduces cobalt nitrate to cobalt. The as-prepared CNFs-Co exhibits one-dimensional straight-arm CNFs that wound around each other and establish an open three-dimensional conductive network, thus facilitating rapid electron/ion transport and electrolyte penetration. Moreover, the added magnetic Co nanoclusters endow CNFs with a larger specific surface area, thus increasing the active sites and facilitating the transportation of Na^+. The density functional theory (DFT) calculation indicates that CNFs-Co has stronger Na^+ adsorption energy. The as-prepared CNFs-Co as anode for SIBs shows a high specific capacity of 246 mAh/g at 0.1 A/g after 200 cycles, and the attenuation is less than 1%. Meanwhile, the initial Coulombic efficiency is 91%. Importantly, the specific capacity of the CNFs-Co anode is 104 mAh/g after 1000 cycles at 10 A/g, and the cycling efficiency exceeds 99%. Moreover, the assembled CNFs-Co||$Na_3V_2(PO_4)_3$ full cell delivers excellent Coulombic efficiency of stabilized above 99% after 200 cycles and a high specific capacity of 185 mAh/g.

Fig. 1a illustrates the feasible manufacturing process for *in-situ* CNFs growth on Al foils. Firstly, CNFs were directly grown on Al foil (4×150 cm^2) through RTR-PECVD method, which could realize a single batch production (Fig. S1 in Supporting information). The CNFs grown for 60 min exhibited uniform straight-arm fiber morphology with a diameter of ~70 nm (Fig. S2 in Supporting information). Secondly, the CNFs were soaked in cobalt nitrate solution and were reduced in H_2 atmosphere for 1 h. As exhibited in Fig. 1 and Fig. S3 (Supporting information), the CNFs-Co still exhibit an uniform straight arm morphology with a diameter of approximately 100 nm. Meanwhile, the C and Co are homogeneously distributed in CNFs-Co (Fig. 1e). To further distinguish the microstructure of CNFs-Co, transmission electron microscope (TEM) characterizations were conducted. The lattice distance of 0.20 nm for the (111) crystal plane of Co nanoclusters was observed in Fig. 1d, which is strongly supported by the selected area electron diffraction (SAED) pattern (inset in Fig. 1d) [21]. Around Co nanoclusters, the carbon interplaner crystal spacing (0.39 nm) is larger than that of graphite (0.33 nm) [22]. Moreover, many vacancy defects formed in the CNFs-Co (green circles in Fig. 1d), thus providing more active sites for the adsorption of Na^+ [23].

The X-ray diffraction (XRD) pattern of the as-prepared CNFs shows two broad diffraction peaks (Fig. 2a), which correspond to the (002) and (100) planes of graphite, respectively [24]. And the broadness indicates the amorphous feature of CNFs. The CNFs-Co shows a similar XRD pattern with CNFs and no peaks for Co were detected. This result is suggesting a trace amount of added Co. In addition, Raman spectra in Fig. 2b shows two typical D and G bands at 1340 and 1598 cm^{-1} in both CNFs-Co and CNFs. This bands are ascribed to the disordered sp^3 carbon for the D band and ordered sp^2 graphitic carbon for the G band, respectively [25]. The D band reflects the defects and disorder degree of carbon while the G band demonstrates the stretching of sp^2. Importantly, the intensity ratio of the G to D band of CNFs-Co ($I_G/I_D = 1.04$) is higher than that of CNF ($I_G/I_D = 1.00$), related to higher graphitization degree of CNFs-Co [26]. As shown in Fig. 2c, a significant weight variation of CNFs-Co was received from a thermogravimetry analysis (TGA), which should be caused by the process of Co oxidizing into Co_3O_4 and carbon combustion in the air atmosphere. The Co content determined from TGA is 0.12% (Fig. S4 in Supporting information), signifying Co nanoclusters in CNFs-Co almost have no contribution to the capacity. This result demonstrates the improved capacity is mainly from the modification of carbon.

X-ray photoelectron spectroscopy (XPS) is an effective way to investigate surface chemistry and composition. As shown in Fig. 2d, two distinct peaks at 285 and 532 eV were observed corresponding to the C 1s and O 1s peaks, respectively. This suggests that CNFs contains C and O elements. Fig. 2e shows the peaks of C 1s in CNFs and CNFs-Co. The C 1s peak can be mainly deconvoluted into four subpeaks at 284.76, 285.1, 286.6, and 287.3 eV, which correspond to C-sp^2, C-sp^3, C–O, and C=O, respectively [27,28]. Compared to CNFs, the graphitization degree of CNFs-Co was improved. The ratio of sp^2/sp^3 of CNFs-Co increased, and the percentage of the sp^2 carbon increased in CNFs-Co relative to CNFs. These XPS results are consistent with the Raman characterizations. The Co 2p XPS spectrum of CNFs-Co shows two split peaks at 778.1 eV and 794.5 eV (Fig. 2f), which can be ascribed to metallic Co (Co^0). Moreover, other valence state species for Co can also be observed, which are associated with the partially oxidized Co nanoclusters [29].

The first discharge cycle for CNFs-Co features a distinct irreversible peak at 0.7 V (Fig. 3a). This phenomenon corresponds to electrolyte decomposition and the formation of a solid electrolyte interface (SEI) film on the electrode surface. The SEI may lead to partial Na^+ consumption and electrolyte degradation [30]. The curves occur overlap almost completely in the following cycles, indicating the formed SEI film has stabilized. As shown in Fig. 3b and Fig. S5 (Supporting information), the formed SEI film becomes stable in the second cycle CV curves for both CNFs-Co and CNFs in the voltage range of 0.01–3.0 V at 0.1 mV/s. Similarly, the discharge/charge voltage profiles of CNFs-Co at 0.1 A/g exhibit overlap except for the first curve, which shows that the CNFs-Co electrode has excellent reversibility. Moreover, an ester-based electrolyte was

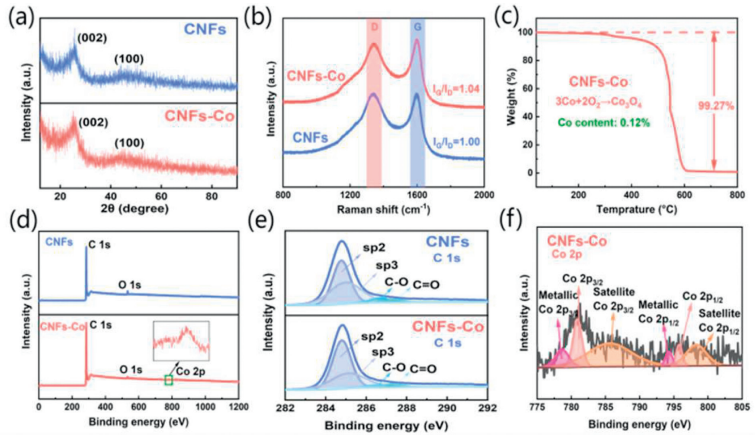

Fig. 2. Phase and electronic structure measurements for CNFs-Co and CNFs. (a) XRD pattern, (b) Raman spectra, (c) TGA curve, (d) XPS survey spectra of CNFs and CNFs-Co. (e, f) High-resolution XPS spectrum of C 1s and Co 2p.

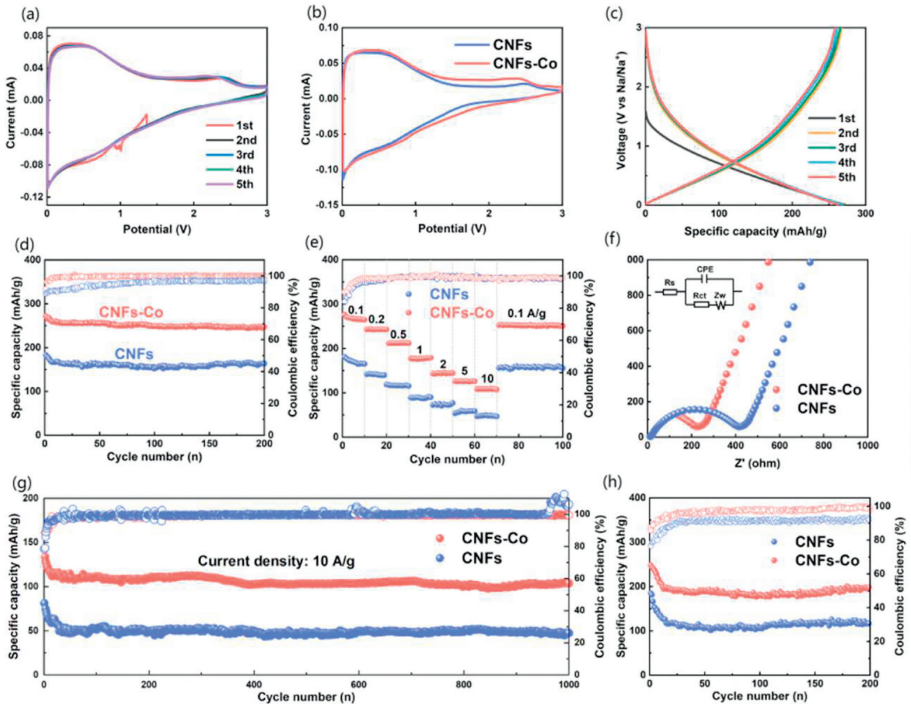

Fig. 3. Electrochemical properties of CNFs-Co and CNFs. (a) CV curves of CNFs-Co at 0.1 mV/s. (b) Second cycle CV curves at 0.1 mV/s. (c) Discharge/charge voltage profiles of CNFs-Co at 0.1 A/g. (d) Cycle performance at 0.1 A/g. (e) Rate capability. (f) EIS spectra. (g) Long-term cycling performance at 10 A/g and (h) Cycle performance of the full cell at 0.1 A/g.

used to operate SIBs (Fig. S6 in Supporting information) and to reveal the universality of CNFs-Co and CNFs anode materials in different types of electrolytes. A similar property change trend in the diglyme-based and ester-based electrolytes was obtained, further confirming the stability of the prepared anode materials.

Benefiting from the superior kinetic synergy of the added Co and diglyme-based electrolyte, CNFs-Co shows excellent long-term cycling performance at 0.1 A/g than that of CNFs (Fig. 3d). Compared with the ester-based electrolyte (Fig. S6d), the initial Coulombic efficiency of CNFs-Co in the diglyme-based electrolyte improves from 87% to 91%. After 200 cycles, a high specific capacity of 246 mAh/g with a low capacity fading rate is obtained and the Coulombic efficiency is over 99%. Conversely, the CNFs anode exhibits an unstable-low specific capacity (157 mAh/g) and Coulombic efficiency (97%). Thus, CNFs-Co exhibits excellent sodium storage capability and stable cycling performance than that of CNFs. Furthermore, the high-rate capability of CNFs-Co is superior to CNFs, which can be attributed to its outstanding conductivity, effective adsorption, and enhanced reaction kinetics (Fig. 3e). In a CNFs-Co cell, with the stepwise increasing current density from 0.1, 0.2, 0.5, 1.0, 2.0, 5.0 A/g to 10.0 A/g, the corresponding average discharge capacity declined from 264, 243, 212, 176, 145, 125 mAh/g to 108 mAh/g, respectively. More promisingly, the CNFs-Co cell shows a remarkable structural stability and the capacity reverses to 251 mAh/g as the current density returns to 0.1 A/g. In contrast, the CNFs cell shows a rapid capacity decay with the current density increase, while delivers a inferior discharge capacity of 51 mAh/g at 10 A/g. The fast reaction kinetics of CNFs-Co can be further confirmed by the electrochemical impedance spectroscopy (EIS). As shown in Fig. 3f, the Nyquist plots consist of a sloping straight line in the low-frequency region and a semicircle in the high-frequency region, which are con-

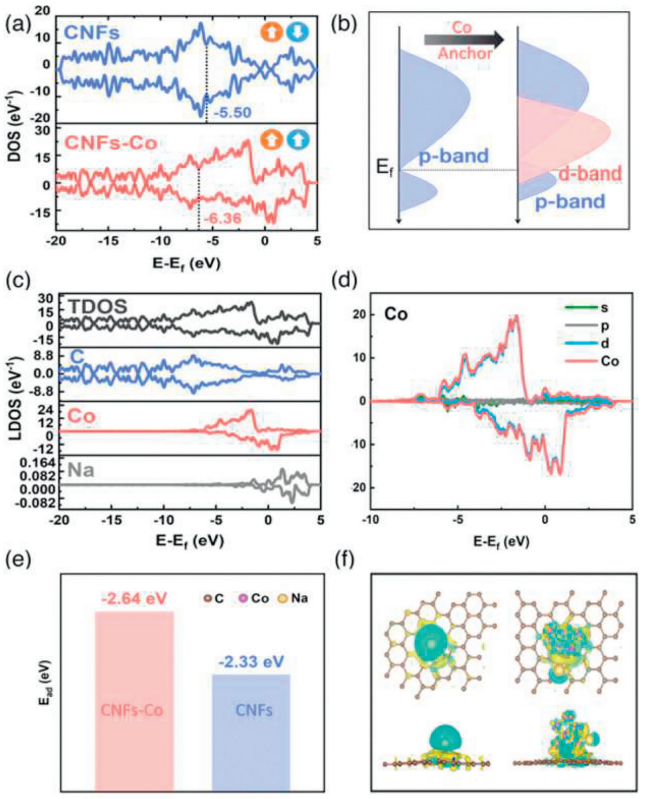

Fig. 4. Theoretical calculations of CNFs-Co and CNFs. (a) The total density of states (TDOS) and p-band center. (b) Electron orbital diagram. (c) DOS of CNFs-Co. (d) Projected DOS (PDOS) of Co. (e) Adsorption energy of Na ion and (f) The difference charge density of Na^+ absorbed on different carbon structures (Yellow and blue regions represent charge accumulation and depletion, respectively. Brown, pink, and yellow balls represent C, Co, and Na atoms, respectively).

trolled by diffusion and charge transfer, respectively [31]. Combing the equivalent circuit model (inset in Fig. 3f), the charge transfer resistance (R_{ct}) of the CNFs-Co is determined to be 220 Ω and lower than that of CNFs, suggesting the enhanced electron transfer ability. A gradual increase capacity for CNFs-Co is observed in the first 300 cycles (Fig. 3g), and a new irreversible SEI film gradually forms on its surface as the cycles operating at 10 A/g. The CNFs-Co shows remarkable cycling stability for high-power SIBs, which possesses high specific capacity with 104 mAh/g after 1000 cycles and a high Coulombic efficiency with 99.9%. Whereas, an unstable specific capacity (51 mAh/g) and Coulombic efficiency are obtained in CNFs cell. To verify the practical Coulombic efficiency of the CNFs-Co battery, we assembled CNFs-Co||$Na_3V_2(PO_4)_3$ full cells, in which all electrodes had been activated before using (Fig. 3h). The CNFs-Co||$Na_3V_2(PO_4)_3$ full cells show excellent Coulombic efficiency that exceeds 99% even after 200 cycles and high discharge specific capacity of 185 mAh/g. A poor specific capacity (110 mAh/g) and Coulombic efficiency (92%) are received in CNFs||$Na_3V_2(PO_4)_3$ full cells. These results suggest that the added spin state Co nanoclusters improve the electrochemical performance of CNFs for SIBs.

To further reveal the high-efficiency sodium storage mechanism of CNFs-Co, DFT calculations were conducted to explore how Co nanoclusters affect Na^+ adsorption behavior. Per the previous studies [15], Na^+ tends to preferentially adsorbed at the vacancy defects of CNFs. Anchoring spin state Co nanoclusters at the vacancy defects (Fig. S7 in Supporting information), the order degree of lattice structure around Co would be improved, which provides a channel for the rapid transport of Na^+. The total density of states (TDOS) and p-band center of C were calculated to deeply explain how the related physical parameters influence SIBs. The CNFs-Co exhibits a higher TDOS near the Fermi level than that of CNFs (Fig. 4a), improves Na^+ storage capacity and increases electronic conductivity. As shown in Fig. 4b, the added Co induces the orbital hybridization of C p and Co d, thus downshifting the p-band center of C from −5.50 eV in CNFs to −6.36 eV in CNFs-Co. The lower p-band center suggests the partially filled anti-bonding state of C orbital, revealing the anchored magnetic Co nanoclusters can optimize the adsorption of Na^+ on the carbon active sites in CNFs-Co. Meanwhile, the high p-band center in CNFs means the empty anti-bonding state of C, thus exhibiting a weak Na^+ adsorption. Furthermore, the introduction of Co leads to spin polarization near the Fermi level in DOS of C, manifesting as the asymmetric distribution of spin up and spin down in the DOS (Figs. 4a and c). In Figs. S8b and S9a (Supporting information), the state projected density (PDOS) of C is mainly contributed by p orbital, and the anchored magnetic Co nanoclusters caused asymmetric distribution of the PDOS of C p orbital. Importantly, the spin polarization states near the Fermi level mainly result from the Co d orbital, which mainly contributes conduction band rather than valence band (Fig. 4d). The state density of other elements in CNFs and CNFs-Co is shown in Figs. S8 and S9 (Supporting information). To clarify the correlation mechanism between p-band center of C and cyclic stability, we calculated the adsorption energy of Na^+ on CNFs-Co and CNFs. The adsorption energy ($\triangle E_{ad}$) of Na^+ on CNFs-Co is −2.64 eV (Fig. 4e), which is lower than that of CNFs (−2.33 eV). This result demonstrates a more strengthened Na^+ adsorption derived form the influence of spin state Co. The difference in charge density caused by spin state cobalt leads to substantial electron redistribution at active sites, which further proves the improved Na^+ adsorption (Fig. 4f). Meanwhile, Na^+ adsorbed on carbon site exhibits a higher electron transfer efficiency than that of Co site. The above DFT calculations confirm that spin state Co could modulate the p-band center of carbon and promote the Na^+ adsorption.

In summary, CNFs anchored with magnetic Co nanoclusters exhibit outstanding physicochemical properties. The CNFs-Co features large interplanar spacing (0.39 nm) and abundant vacancy defects. The spin state Co downshifts the p-band center of carbon and then promotes the adsorption of Na^+. The CNFs-Co anode exhibits excellent sodium storage performance with a high power property with 108 mAh/g after 1000 cycles at 10 A/g. This study provides a novel strategy for developing high performance anode materials for SIBs.

Declaration of competing interest

The authors declare that they have no known competing financial interests or personal relationships that could have appeared to influence the work reported in this paper.

Acknowledgments

This work was financially supported by the National Natural Science Foundation of China (Nos. 52271011, 52102291). We would like to thank the Analytical & Testing Center of Tiangong University For Transmission Electron Microscope work.

Supplementary materials

Supplementary material associated with this article can be found, in the online version, at doi:10.1016/j.cclet.2023.109106.

References

[1] J.Y. Hwang, S.T. Myung, Y.K. Sun, Chem. Soc. Rev. 46 (2017) 3529–3614.
[2] M. Du, K.D. Du, J.Z. Guo, et al., Rare Metals 42 (2023) 1603–1613.
[3] Z. Zhang, G. Xie, Y. Chen, et al., J. Mater. Sci. Technol. 171 (2024) 16–23.
[4] Y. Jiao, Y. Zheng, K. Davey, et al., Nature Energy 1 (2016) 1–9.

[5] S.M. Zheng, Y.R. Tian, Y.X. Liu, et al., Rare Metals 40 (2021) 272–289.
[6] Z. Zhang, Y. Chen, S. Sun, et al., J. Mater. Sci. Technol. 119 (2022) 167–181.
[7] Z.Y. Yu, Q. Sun, H. Li, et al., Rare Metals 42 (2023) 2982–2992.
[8] R. Zhang, H. Chen, H. Yue, Chin. Chem. Lett. 34 (2023) 107580.
[9] Y. Tong, Y. Wu, Z. Liu, et al., Chin. Chem. Lett. 34 (2023) 107443.
[10] R. Xu, Z. Yi, M. Song, et al., Carbon 206 (2023) 94–104.
[11] H. Yang, Z. Zhang, Z. Yu, et al., Mater. Lab 1 (2022) 220016-1-220016-13.
[12] X. Ma, Z. Zhang, J. Wang, et al., Rare Metals 40 (2021) 2802–2809.
[13] J. Gou, Z. Qiao, Z. Yu, et al., Surf. Innov. 11 (2022) 70–78.
[14] S. Chen, D. Ren, M. Zhang, et al., Solid State Ionics 327 (2018) 52–58.
[15] C. Li, Z. Zhang, Y. Chen, et al., Adv. Sci. 9 (2022) 2104780.
[16] Y.R. Liu, Z.W. Lei, R.P. Liu, et al., Rare Metals 42 (2023) 1557–1569.
[17] Y. Wen, K. He, Y. Zhu, et al., Nat. Commun. 5 (2014) 4033.
[18] Z. Li, C. Bommier, Z.S. Chong, et al., Adv. Energy Mater. 7 (2017) 1602894.
[19] Q. Ren, Z. Shi, L. Yan, et al., J. Mater. Chem. A 8 (2020) 19898–19907.
[20] D.L. Ba, W.H. Zhu, Y.Y. Li, et al., Rare Metals 41 (2022) 4075–4085.
[21] Z. Wang, J. Shen, S. Ji, et al., Small 16 (2020) 1906634.
[22] H. Yang, S. Zhou, B. Zhang, et al., Adv. Funct. Mater. 31 (2021) 2102280.
[23] Y. Wei, Y. Wang, X. Zhang, et al., ACS Appl. Mater. Interfaces 12 (2020) 35058–35070.
[24] Z. Chen, R. Wu, Y. Liu, et al., Adv. Mater. 30 (2018) 1802011.
[25] Y. Wei, B. Wang, Y. Zhang, et al., Adv. Funct. Mater. 31 (2021) 2006033.
[26] Y. Wang, Y. Wei, B. Wang, et al., Carbon 177 (2021) 60–70.
[27] R. Guo, C. Lv, W. Xu, et al., Adv. Energy Mater. 10 (2020) 1903652.
[28] J. Qian, F. Wang, Y. Li, et al., Adv. Funct. Mater. 30 (2020) 2000742.
[29] L. Tao, Q. Wang, S. Dou, et al., Chem. Commun. 52 (2016) 2764–2767.
[30] S. Choi, Y. Ko, J. Lee, et al., Adv. Funct. Mater. 25 (2015) 1780–1788.
[31] T. Zhang, F. Ran, Adv. Funct. Mater. 31 (2021) 2010041.